Slag Accumulation in the Titan Solid Rocket Motor Upgrade

W. A. Johnston,* J. W. Murdock,† S. Koshigoe,* and P. T. Than‡
The Aerospace Corporation, El Segundo, California 90009-2957

Numerical simulations of slag accumulation in the aft end of the Titan solid rocket motor upgrade (SRMU) are described. These quasisteady, two-phase flow solutions at 0-, 30-, 55-, 80-, 110-, and 125-s burnback geometries involve a gas phase and an Al_2O_3 liquid phase of a single droplet size, where four droplet sizes (10, 35, 60, and 100 μm) have been considered. The two-phase flow calculations are inviscid and rotational (Euler equations), with full momentum and energy coupling between the phases. Both phases are treated with an Eulerian approach. The stability of the Al_2O_3 droplets with respect to breakup is shown not to affect our predictions. The capture rate as a function of time is determined from the solutions at the five burn times, which is then integrated over the total burn time to determine the total slag captured. It is found that slag capture starts at time zero and continues throughout the firing. Using a droplet size distribution from a recent experimental study produces a total slag accumulation of 2265 kg, which is in good agreement with the static test results. Also, predictions of the slag pool depth as a function of time show good agreement with real-time radiography measurements. Small changes in propellant grain design, such as the use of a short-lived inhibitor in the submerged nozzle region, only provide a small reduction in the total slag captured during the burn. Slag accumulation is unaffected by the g levels typical of an SRMU flight.

Nomenclature

C_D	=	liquid droplet drag coefficient
D	=	liquid droplet diameter
e	=	total energy per unit volume for the gas, $p/(\gamma - 1) + (\frac{1}{2})\rho(u^2 + v^2)$
e_k	=	total energy per unit volume for the liquid droplet phase
F, F_k	=	flux variables defined by Eqs. (1) and (8)
G, G_k	=	flux variables defined by Eqs. (1) and (8)
g	=	body force acceleration, in the z direction
H, H_k	=	source terms defined by Eqs. (1) and (8)
K	=	propellant burn rate constant
n	=	propellant burn rate exponent
Pr	=	Prandtl number
p	=	gas pressure
p_{ref}	=	reference pressure
$p_{surface}$	=	propellant surface pressure
r	=	radial coordinate
t	=	time
T	=	gas temperature
T_k	=	liquid droplet temperature
U, U_k	=	conserved dependent variables defined by Eqs. (1) and (8)
u, v	=	velocity components in the r, z directions
u_k, v_k	=	liquid droplet velocity components in the r, z directions
u_n	=	velocity normal to the surface
We	=	Weber number
z	=	axial coordinate
α	=	heat transfer coefficient of the liquid droplet
γ	=	gas specific heat ratio
μ	=	gas viscosity
ρ	=	gas density
ρ_d	=	liquid droplet density
ρ_k	=	mass per unit volume of the droplet phase (number density times droplet mass)
ρ_{prop}	=	propellant density
σ	=	surface tension for Al_2O_3

I. Introduction

SOLID rocket motors with metallized propellants and submerged nozzles tend to accumulate significant amounts of slag in the region around the nozzle. Since the slag retained in this manner is dead weight, slag accumulation constitutes a degradation of motor performance and is undesirable. Furthermore, sloshing or ejection of this molten liquid slag can lead to control problems and possible vehicle instability. For these reasons, an appropriate design goal for solid rocket motors is to accumulate as little slag as possible. For large segmented solid rocket motors with submerged nozzles, such as the Space Shuttle solid rocket booster (SRB) and the Titan solid rocket motor upgrade (SRMU), the amount of slag accumulation during the total burn can be considerable. Values for the Shuttle SRB of as much as 1600 kg have been reported[1] during horizontal static firings. Since molten slag may well have spilled out of the SRB motor because of its orientation during this static firing, the slag accumulated during flight may be greater. During each of the five vertical test firings of the Titan SRMU that have been carried out to date (PQM1', QM1, QM2, QM3, and QM4), more than 1800 kg of slag were captured.

In an attempt to better understand the flow situation inside the Titan SRMU that produced these slag accumulations, we have carried out a series of numerical simulations of the two-phase flow in the aft end of this motor. The two-phase flow solutions involve a gas phase and an Al_2O_3 liquid phase of a single droplet size. A schematic diagram of the SRMU showing the initial (zero burnback) geometry is found in Fig. 1. The location at which the slag accumulates as a molten slag pool is indicated in this figure.

Quasisteady, axisymmetric numerical solutions for six burnback geometries (0, 30, 55, 80, 110, and 125 s) that span the total burn time of 135 s, and four different droplet sizes (10, 30, 60, and 100 μm), have been carried out. The solutions for the different burnbacks enable us to examine how the slag
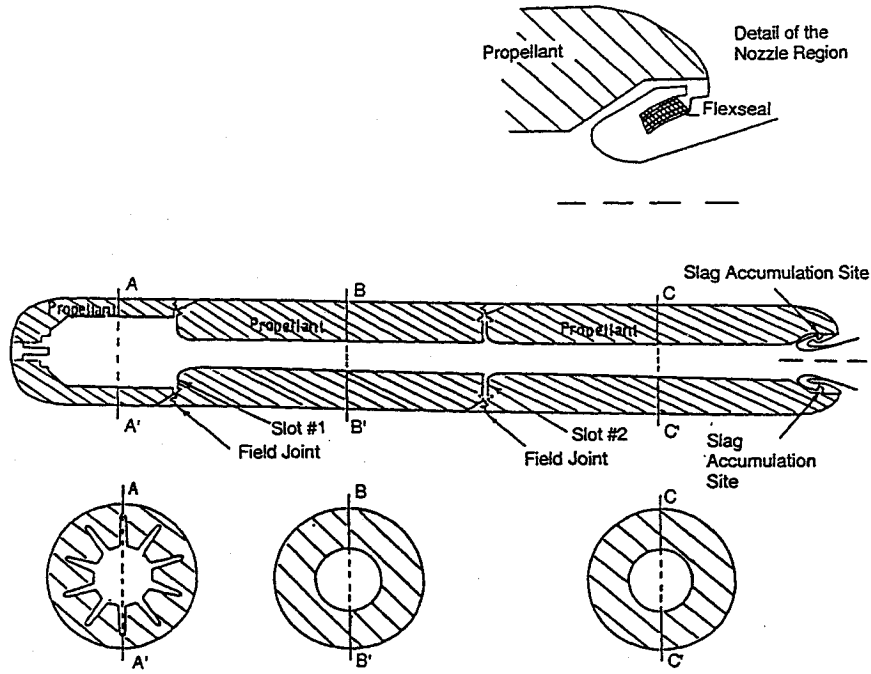
Fig. 1 Initial geometry for Titan SRMU.

capture rate varies with time, and to predict the total amount of slag accumulation by integrating the slag capture rate over the total burn. The two-phase flow calculations are inviscid and rotational (Euler equations), with full momentum and energy coupling between phases; both phases are treated within an Eulerian framework. The treatment of the gas phase as inviscid and rotational flow, rather than potential flow, is required for the accurate treatment of fluid motion in solid rocket motors.[2] The governing equations and boundary conditions are discussed in Sec. II. The numerical solution of this boundary value problem employs a code developed by Misterek et al.,[3] which in turn is based on the time-marching, finite volume, total variation diminishing (TVD) method.[4,5] Numerical results for the cases already described may be found in Sec. III, along with some additional results that pertain to the effect of vehicle acceleration and some design modifications on the slag accumulation. Also in Sec. III, the issues of droplet instability and breakup are discussed, and some related numerical results are presented. The results are summarized in Sec. IV.

II.   Theory

The axisymmetric governing equations for the gas phase of this two-phase flow may be written as

$$\frac{\partial U}{\partial t} + \frac{\partial F}{\partial r} + \frac{\partial G}{\partial z} + H = 0 \tag{1}$$

where

$$U = r\begin{bmatrix} \rho \\ \rho u \\ \rho v \\ e \end{bmatrix}, \qquad F = r\begin{bmatrix} \rho u \\ \rho u^2 + p \\ \rho u v \\ u(e + p) \end{bmatrix}, \qquad G = r\begin{bmatrix} \rho v \\ \rho u v \\ \rho v^2 + p \\ v(e + p) \end{bmatrix}$$

$$H = \begin{bmatrix} 0 \\ -p + rM_k(u - u_k) \\ rM_k(v - v_k) \\ rM_k[v_k(v - v_k) + u_k(u - u_k)] + rE_k(T - T_k) \end{bmatrix}$$

Also, M_k and E_k represent the interphase momentum and energy transfer between the gas phase and a liquid droplet phase. Following Ref. 3, we write the drag between the gas and liquid droplet phases as

$$M_k = (3\mu\rho_k/4D^2\rho_d)C_D Re_k \tag{2}$$

The Reynolds number of the gas flow relative to the droplet is defined as

$$Re_k = \frac{\rho D\sqrt{(u - u_k)^2 + (v - v_k)^2}}{\mu} \tag{3}$$

The viscosity is expressed in the form

$$\mu = \mu_{Ref}(T/T_{Ref})^{0.65} \tag{4}$$

with $T_{Ref} = 3537$ K and $\mu_{Ref} = 897.3$ mPa·s, and the drag coefficient is expressed as[6]

$$C_D = 24/Re_k \quad \text{for} \quad Re_k \leq 0.34$$
$$= 0.48 + 28/Re_k^{0.85} \quad \text{for} \quad Re_k > 0.34 \tag{5}$$

Following Ref. 3, we write the energy exchange parameter as

$$E_k = 6\alpha\rho_k/D\rho_d \tag{6}$$

where α is expressed in terms of a Nusselt number as[7]

$$Nu = 2 + 0.6Pr^{0.33}Re_k^{0.5} \tag{7}$$

and where the Prandtl number is 0.72 and various gas, propellant, and liquid Al_2O_3 properties are found in Table 1.

The governing equations for the liquid droplet phase may be written as

$$\frac{\partial U_k}{\partial t} + \frac{\partial F_k}{\partial r} + \frac{\partial G_k}{\partial z} + H_k = 0 \tag{8}$$

where

$$U_k = r \begin{bmatrix} \rho_k \\ \rho_k u_k \\ \rho_k v_k \\ e_k \end{bmatrix}, \qquad F_k = r \begin{bmatrix} \rho_k u_k \\ \rho_k u_k^2 \\ \rho_k u_k v_k \\ u_k e_k \end{bmatrix}, \qquad G_k = r \begin{bmatrix} \rho_k v_k \\ \rho_k u_k v_k \\ \rho_k v_k^2 \\ v_k e_k \end{bmatrix}$$

$$H_k = \begin{bmatrix} 0 \\ -rM_k(u - u_k) \\ \rho_k g - rM_k(v - v_k) \\ \rho_k v_k g - rM_k[v_k(v - v_k) + u_k(u - u_k)] - rE_K(T - T_k) \end{bmatrix}$$

The flow solutions are obtained in this study with a time-marching, finite volume, two-phase flow code.[3] This code employs a numerical procedure described in detail in Refs. 4 and 5, which in turn is based on the TVD methodology of Harten.[8] The TVD methodology ensures that the flow solution is spatially second-order accurate, and that large gradients or discontinuities present in the flowfield are resolved without wiggles or excessive smearing. Although time-marching solutions are performed in this study, only the steady flow that is the asymptotic limit of a calculation is of interest. Since time-accurate solutions are not required, both explicit and implicit time-stepping schemes have been used to economize the calculations. The finite volume cell mesh for the Titan SRMU in its zero burnback configuration, which is shown in Fig. 2, illustrates the type of grids used in this study. Since the flow is axisymmetric, we consider only a portion of the internal flow passage that is bounded below by the centerline. The cell mesh extends in the axial direction, from a location

Table 1 Gas, propellant, and liquid Al₂O₃ properties

γ, gas	1.2
R, gas	424.3, N·m/kg·K
T_{flame}, gas	3537, K
ρ_{prop}, propellant	179.4, Mg/m³
K, propellant	8.00, mm/s
n, propellant	0.3
p_{ref}	6.89, MPa
ρ_l, Al₂O₃	19, Mg/m³
σ, Al₂O₃	0.438, N/m

somewhat downstream of slot 2, to a short distance downstream of the nozzle throat. Also, the grid extends radially from the centerline out to the propellant surface or the slot/nozzle wall. In an attempt to simplify the complicated geometry of the flow passage far inside the slot where there is very little flow, some geometric modifications have been made; in particular, the stagnant region adjacent to the nozzle flexseal (see Fig. 1) is ignored for the flow calculation (but not for the slag pool depth calculation). The grid shown is a multi-block grid, consisting of two blocks, that was created using elliptic grid generation techniques.[9]

Several types of boundary conditions occur along the border of the computational domain. The portion of the boundary that connects points A and B in Fig. 2 is a subsonic inflow boundary. Combustion gas laden with Al₂O₃ droplets that is generated farther forward in the motor enters the domain across this portion of the boundary. At this location we specify the normal mass flow rate, the stagnation enthalpy, and zero tangential velocity for the gas phase and apply a characteristics formulation.[10] The mass flow rate was obtained from an axisymmetric, single-phase flow solution for the zero burnback Titan SRMU.[11] The liquid droplet phase is assumed to be in thermal and velocity equilibrium with the gas phase at this boundary and is assigned a 34% fraction of the total entering mass flow. This mass fraction, which depends on the propellant formulation, was obtained for the Titan SRMU using the SPP code.[12]

The portion of the boundary that connects points B and C is the burning propellant surface. This surface also is a subsonic inflow boundary, and the treatment here is similar to the AB section. However, the gas phase mass flow rate off the burn surface is not specified as before, but is calculated from the relation

$$(\rho u_n)_{\text{surface}} = \rho_{\text{prop}} K (p_{\text{surface}}/p_{\text{ref}})^n \qquad (9)$$

where values for the constants may be found in Table 1.

Moving from point C to point D in Fig. 2, the boundary coincides first with exposed casing insulation, and subsequently, with the nozzle wall. Both of these are solid, impermeable surfaces. For the gas phase, the only mathematical requirement is that the normal velocity component at the surface be zero. This requirement is met with a simple treat-
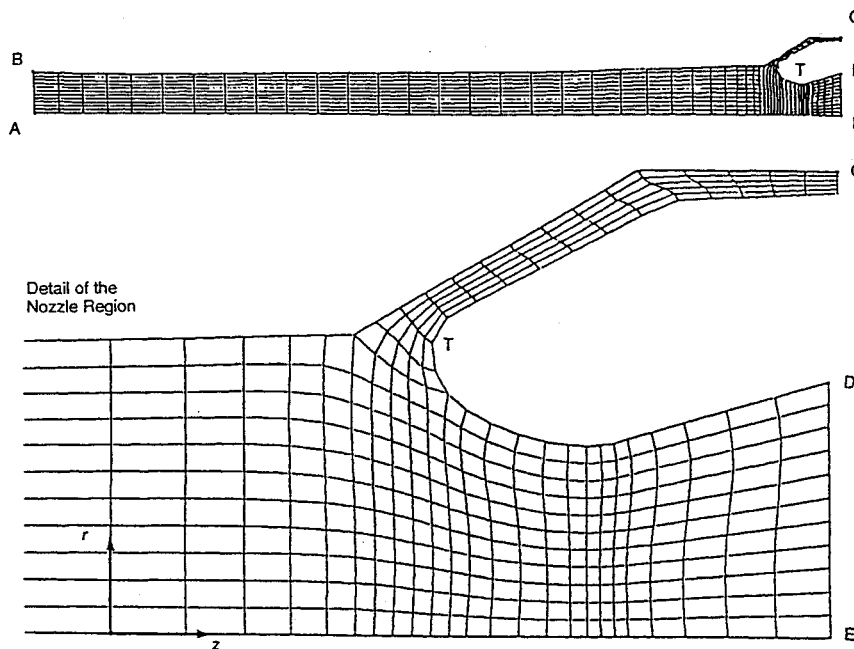

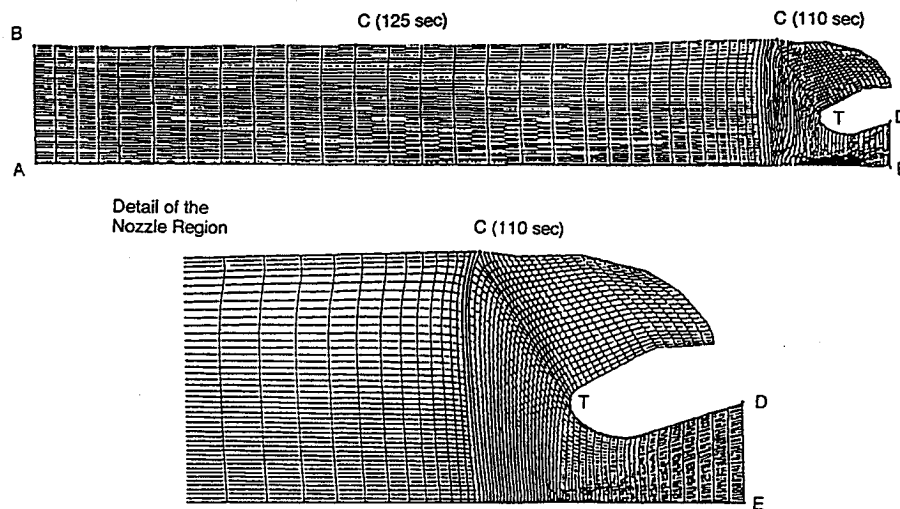Fig. 2 Grid mesh, aft end of Titan SRMU (0-s burnback).

Fig. 3 Grid mesh, aft end of Titan SRMU (110- and 125-s burnback).

ment based on one-dimensional wave reflections due to Reddall.[11] For the liquid droplet phase, this boundary is treated as impermeable (no-flux), if the normal droplet velocity in the cell adjacent to the surface is directed away from the surface; i.e., the treatment is the same as the gas phase in this case. However, if the normal droplet velocity adjacent to the surface is towards the surface, it is assumed that droplets will impinge on the surface and be captured. In this case, the surface acts essentially as an outflow boundary for droplets. The treatment of this absorbing boundary follows Ref. 3; the mass flux at the wall is calculated, and that mass is assumed to exit the flowfield. The rate of droplet mass capture is integrated from point C to point T at the top of the nozzle (see Fig. 2), to give the rate of slag accumulation for the total motor. (It is assumed that droplets captured between C and T will collect in a pool of molten liquid Al_2O_3 at the bottom of the submerged region, while droplets captured between T and D will drain out the nozzle.)

Between points D and E, there is supersonic outflow from the computational domain. Here, the mathematical problem requires no boundary conditions for either the gas or the droplet phase; numerical boundary conditions are obtained by extrapolating all flow variables from upstream. Finally, the centerline of this axisymmetric calculation lies between points E and A.

Computational meshes for the flow geometries at 30, 55, 80, 110, and 125 s of burnback were also created. The mesh used for the 110- and 125-s calculations is shown in Fig. 3. The points labeled in Fig. 2 (A, B, C, D, E, and T) to assist the reader in locating the extent of the burning propellant surface, slag capture region, etc., are indicated also in Fig. 3. It may be seen that the same grid is used for both 110 and 125 s of burnback, the only geometrical difference being the location of point C, which marks the extent of the burning propellant.
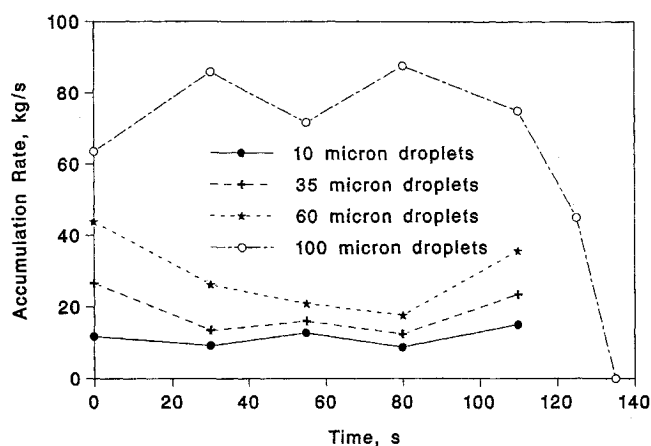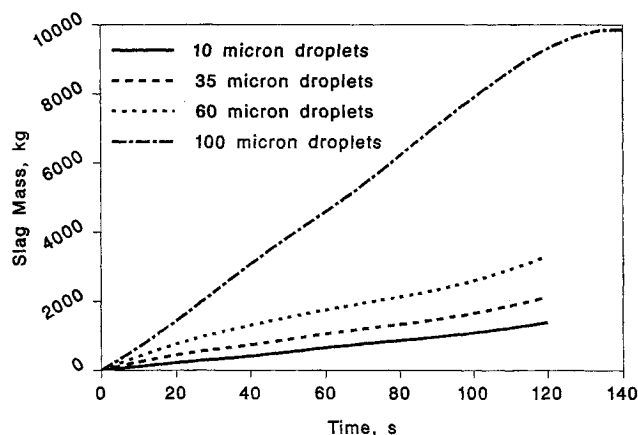
III. Numerical Results

In this section, numerical results from several flow simulations are presented. Quasisteady solutions for 0, 30, 55, 80, 110, and 125 s of burnback have been carried out for two-phase flows where all the Al_2O_3 is assumed to form droplets of a single, uniform size (10, 35, 60, or 100 μm in diameter). The choice of droplet sizes considered in this work was motivated initially by the results of several studies,[13,14] which suggest that mean droplet sizes of 1–50 μm characterize the flow in solid rocket motors with aluminized propellants. In particular, Price,[14] citing various authors, discusses the bimodal nature of Al_2O_3 droplet size distributions, with the

droplets being primarily smoke (<2 μm) and secondarily large droplets (5–50 μm). However, we eventually followed Ref. 1 and assumed the presence of somewhat larger droplets (100 μm). The grid meshes range in size from 614 cells for the initial configuration to 3827 cells for the 110- and 125-s burnback geometries. These solutions, which were performed on the Cray II computer at the Phillips Laboratory Supercomputer Center, Kirtland Air Force Base, required from 1 h of CPU time for the easiest case (10-μm droplets and 0 s of burnback) to approximately 10 h of CPU time for the most difficult case (100-μm droplets and 110 s of burnback). However, the figure of 10-h CPU time for the last case is actually an estimated time required to converge that solution from a crude initial guess. In practice we would try to use a good initial guess (e.g., the converged solution for 60-μm droplets on the 110-s burnback mesh) to start the calculation; this can reduce the run time by more than half. Since it was our intention to carry out four solutions, corresponding to the four different droplet sizes, at each burnback geometry, we have achieved significant computational economy by using a converged solution as the initial guess in the subsequent calculation at the same burnback. Memory requirements ranged from 3 to 7 MWords in these solutions.
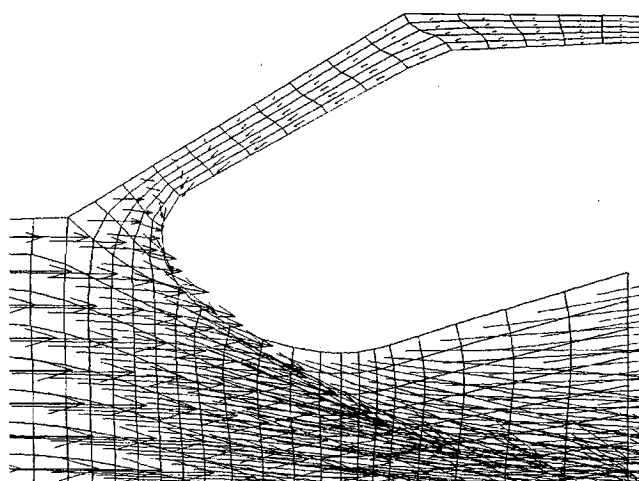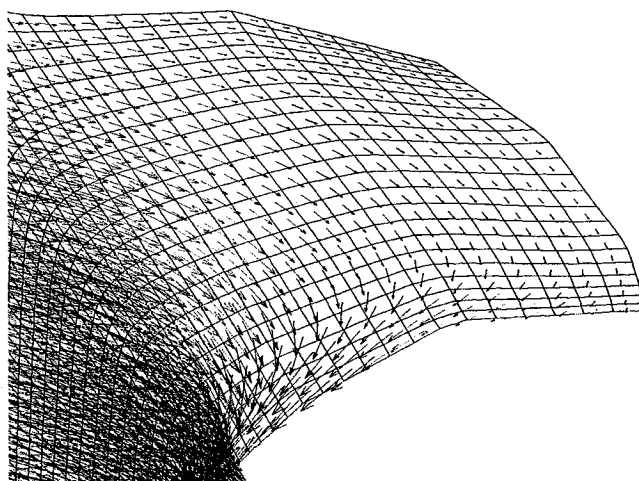
The results from these numerical solutions are summarized in Table 2 and plotted in Fig. 4. In each case the calculation was performed with all of the available slag going to make up the specified drop size. We wish to emphasize two main features of the plots of slag accumulation rate vs time that appear in Fig. 4. First, the slag accumulation rate increases uniformly with droplet size for all burnback times. Second, the slag accumulation rates for all of the assumed droplet sizes are, to a first order of approximation, constant with time before 110 s, when motor tailoff begins. Clearly, these curves are not exactly constant in time prior to 110 s, and there is some variation of the slag accumulation rate, which we intend to discuss. However, this variation is a relatively small effect. Therefore, for the purpose of SRMU performance calculations, which require a knowledge of the time history of the onboard slag mass, it is appropriate to assume that slag accumulates at a constant rate and that the onboard slag mass grows linearly with time prior to 110 s (see Fig. 5). Given the uncertainty associated with the true droplet size of the Al_2O_3, this is clearly the best approach. (Of course this assumes that a sufficient volume to retain all of the captured slag is available throughout the burn, and that the molten slag mass does not spill or boil overboard.) In Fig. 5, slag accumulation time histories are displayed for the four droplet sizes; these curves were obtained by performing trapezoidal rule integrations of the areas under the curves in Fig. 4.

Table 2 Slag accumulation rates for various droplet sizes and burnback geometries

Droplet size, μm	Slag accumulation rate, kg/s					
	0 s	30 s	55 s	80 s	110 s	125 s
10	11.9	9.3	12.9	8.9	15.1	——
35	26.6	13.6	16.1	12.5	23.5	——
60	43.9	26.3	21.0	17.7	35.7	——
100	63.6	85.9	71.8	87.7	75.0	45.0

Fig. 4 Slag accumulation rate vs time.

Fig. 5 Slag accumulation time history.

Fig. 6 Droplet velocity vectors in the submerged nozzle region (0-s burnback, 60-μm-diam droplets).

Fig. 7 Droplet velocity vectors in the submerged nozzle region (110-s burnback, 60-μm-diam droplets).

The variation in the slag accumulation rate with time appears to depend in general on the details of the flow pattern at the mouth of the submerged nozzle region (i.e., in the vicinity of point T in Figs. 2 and 3), and this flow pattern is fairly complicated. At this location, the flow that emanates from the slot, merges with the bore flow and turns 180 deg to exit through the nozzle. While it is difficult to explain all the features displayed by all the curves in Fig. 4, we have gained an understanding of the reasons behind some of the features of some of the curves by a careful examination of the flowfield. Consider the 60-μm droplet curve in Fig. 4. This curve exhibits a concave upwards shape, with an accumulation rate that falls off from a large initial value to a minimum at 80 s and then increases late in the burn. The reason for the large initial capture rate may be seen in Fig. 6, where the droplet velocity vectors in the 0-s burnback geometry are shown. The droplet-laden gas flow, which comes off the burn surface in the normal direction, must turn and align itself with the walls in order for it to exit the slot. (Note that the burn surface is the top slot surface in Fig. 6, while

the bottom surface is a nonburning surface.) Since the droplets, due to their greater density, make wider turns than the gas streamlines, they tend to impact the nonburning surface and are captured. It may be seen in Fig. 6 that droplet velocity vectors in cells adjacent to the nonburning surface have a component directed towards the surface; this indicates slag capture. It also may be seen that the flow in the slot is directed out of the slot, and that there is very little tendency for the bore flow to penetrate into the slot. These observations suggest that for flow in the zero burnback geometry with 60-μm droplets, the large slag capture rate is due to the capture of droplets that originate from propellant inside the slot, because of the proximity of the two surfaces. In fact, the numerical results indicate that 85% of the Al_2O_3 that originates on the slot burn surface is captured at this time. As the burn surface recedes with time and the gap widens, however, this large capture rate tends to diminish. Late in the burn the slag accumulation rate begins to increase, which implies that some other effect has come to dominate the process.

In Fig. 7, the droplet velocity vectors for the 110-s burnback geometry are shown. The entire boundary of the flow domain in the submerged nozzle region is a nonburning surface at this time. The dominant feature of the flowfield in this region is the large-scale turning of the outer bore flow towards the nozzle. It may be seen in Fig. 7 that droplet velocity vectors in cells adjacent to the nozzle wall have a component directed towards the wall; this indicates slag capture. Since a large slot

entrance admits a larger amount of bore flow into the slot, which results in a large and faster turning flow, we would expect the slag capture rate to increase as the area of the slot entrance increases. This appears to be the reason why the slag accumulation rate increases with burnback time, late in the burn for the 60-μm droplet flow. Therefore, the accumulation rate falls early in the burn due to the declining importance of the proximity effect, and rises late in the burn due to the increasing importance of the larger slot entrance area. Although the situation appears to be less pronounced for 35- and 10-μm droplets (see Fig. 4), the tendency for the slag accumulation rate to decrease with time at the start of the burn and to increase with time at the end of the burn is still evident in the time histories of these two droplet sizes.

For 100-μm droplets, however, it is not possible to explain the shape of the slag accumulation rate curve (Fig. 4) in such simple terms (except, of course, for the diminished value at 125 s, when the motor is tailing off). We have examined velocity vector plots, similar to Figs. 6 and 7, for the 100-μm droplet flows at the various burnbacks and concluded that very minor changes in the complex flow pattern near point T (Figs. 2 and 3) are partly responsible for the behavior of this rate curve. The shape of the rate curve also may depend on the grid resolution in the vicinity of point T, where a large fraction of the total slag capture occurs early in the burn (see Fig. 8), although less occurs later in the burn (see Fig. 9). In either case, the accumulation rate trends that were evident from the 10-, 35-, and 60-μm droplet time histories have been masked effectively for 100-μm droplets.

In order to predict the total amount of slag collection in the SRMU, it is necessary to make some assumption about the droplet size(s) that are present in the actual motor. We have followed Ref. 1 and assumed a bimodal droplet size distribution. At a pressure of about 7 MPa, which characterizes the aft region in our motor, Ref. 1 suggests a bimodal log-normal droplet size distribution consisting of small droplets with a 1.5-μm mean and large droplets with a 100-μm mean. We have simplified this bimodal droplet size distribution in our case to a flow with just two droplet sizes, namely, 1.5 and 100 μm. Furthermore, we assume that the 1.5-μm particles are too small to contribute to the slag accumulation. For ammonium perchlorate composite (APC) propellant, which appears to be the propellant formulation closest to the SRMU that was considered, Ref. 1 gives mass fractions for the large and small modes of 0.06 and 0.20, respectively. These num-
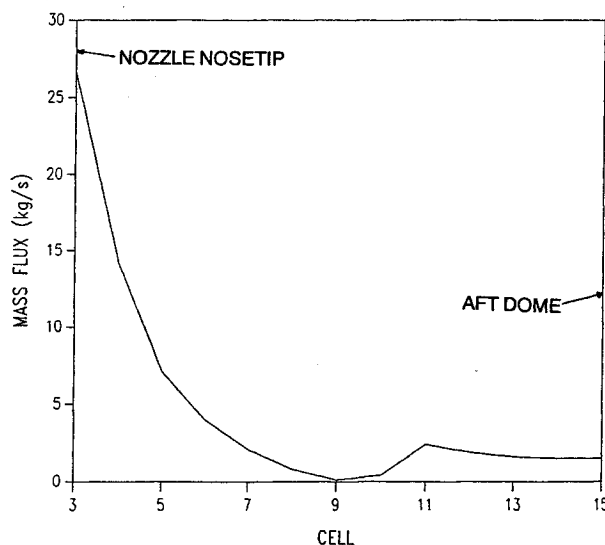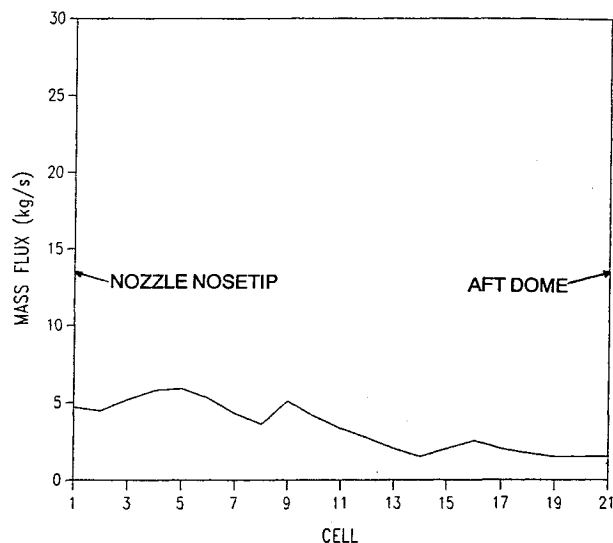

Fig. 9 Slag capture rates for cells with surfaces along the outer wall of the nozzle, 100-μm droplets, 110-s burnback. Note: cells are numbered with increasing distance from point T, cell 1 being adjacent to point T.
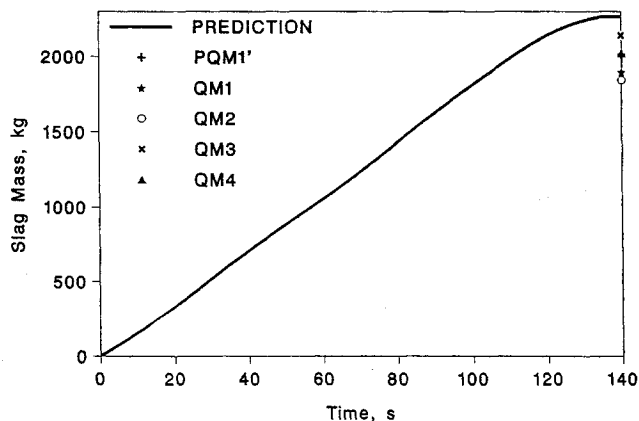

Fig. 10 Slag Accumulation time history; numerical prediction for SRMU. ——— = prediction, ● ● = aerospace data reduction, and ——— = LLNL data.

bers imply that 23% of the Al_2O_3 is in the large-droplet mode, so we simply have scaled the 100-μm droplet results by 0.23 to achieve our projections for the Titan SRMU. These results are shown in Figs. 10 and 11. In Fig. 10, the slag mass in the SRMU vs time is plotted. The numerical results predict a total slag mass of 2265 kg at the end of the burn. This agrees well with the test results of 2015, 1897, 1847, 2141, and 2021 kg for PQM1', QM1, QM2, QM3, and QM4, respectively. In Fig. 11, the numerical prediction for the depth of the SRMU slag pool vs time is shown along with the real-time radiography data reduced by both Aerospace and Lawrence Livermore National Laboratory (LLNL). This result is calculated using a value for the slag density of 19 Mg/m^3 and a value for the volume of the slag repository region based on the true geometry of this region and not the simplified geometry used in our flow calculations. The numerical prediction is in good agreement with real-time radiography measurements of slag depth,[15] taken in the QM2 test during the last half of the burn. In the submerged nozzle region,[16] the distance from the bottom of the slag pool to the top of the nozzle mechanism (point T in Figs. 2 and 3) is about 850 mm, and so this repository region is filled approximately halfway to the top at the end of the burn. These results do not allow for any loss of slag due to spillage or to the violent boiling that occurs subsequent to the burn when the pressure in the motor drops.
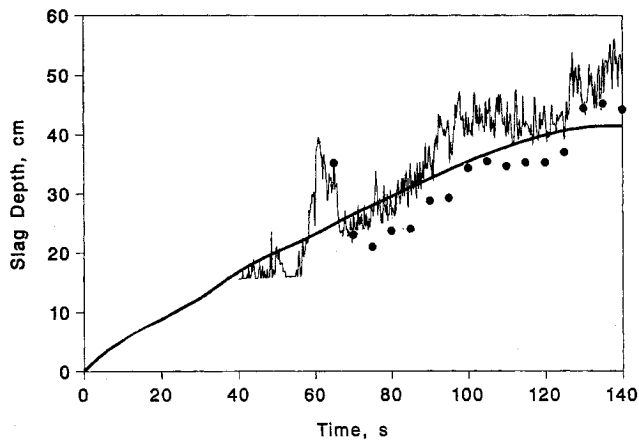

Fig. 8 Slag capture rates for cells with surfaces along the outer wall of the nozzle, 100-μm droplets, 0-s burnback. Note: cells are numbered with increasing distance from point T, cell 3 being adjacent to point T.

Fig. 11   Slag pool depth time history, real-time radiography data collected by LLNL.[15]

Fig. 12   Contours of $We/16$ for 100-μm droplets at 0-s burnback ($We/16 > 1$ indicates instability).

A.   Droplet Stability

We have considered the question of droplet stability with respect to breakup, in that we have checked flow solutions to see if the droplet sizes that were assumed could be maintained. The criterion used for droplet stability is based on the Weber number

$$We = \frac{\rho[(u - u_k)^2 + (v - v_k)^2]D}{\sigma}$$

We have used a conservative (low) value of 438 dyne/cm (Ref. 17) for the surface tension of the liquid Al_2O_3. Following Ref. 18, a critical Weber number is used, above which the droplets are assumed to be unstable; we have set this critical Weber number at 16, which is a conservative (low) value. A contour plot of ($We/16$) is found in Fig. 12 for 100-μm droplets at 0 s of burnback. Where ($We/16$) exceeds 1, the 100-μm droplets are unstable. This area is confined to the nozzle exit region, which implies that droplet breakup occurs only when the flow has passed the region of concern for slag capture. Since 100-μm droplets are the largest considered in this study and since conservative values have been chosen for the surface tension and critical Weber number, this plot and similar ones for the other burn geometries indicate that none of the numerical results presented in this study are invalidated by droplet breakup.

B.   Miscellaneous Results

In addition to the geometric approximation of the flowfield adjacent to the nozzle flexseal that was mentioned previously, we have introduced a second approximation to the geometry by ignoring the intrusion of the slag pool into the computational domain. As the slag accumulates during the burn, the increasing depth of the slag pool corresponds to a decrease in the volume available to the two-phase flow. This effect is negligible early in the burn, but increases with time. To gain some insight as to how greatly this omission would change the calculated slag capture rates, we have carried out a numerical solution for the slag accumulation rate at 55 s of burnback with a 216-mm deep slag pool present. The grid geometries for the flowfield at this time, both with and without the slag pool, are shown in Fig. 13. A depth of 216 mm was chosen as a reasonable depth for the slag pool at 55 s, if approximately 430 mm of slag accumulates linearly over the entire burn. A numerical calculation for a flow with 35-μm droplets in this new geometry yielded a slag accumulation rate of 15.6 kg/s, compared with a corresponding value of 16.1 kg/ s from Table 2, a difference of 3%. Based on this result, and the numerical solutions that show only modest flow at the bottom of the slot, we have concluded that ignoring the geo-
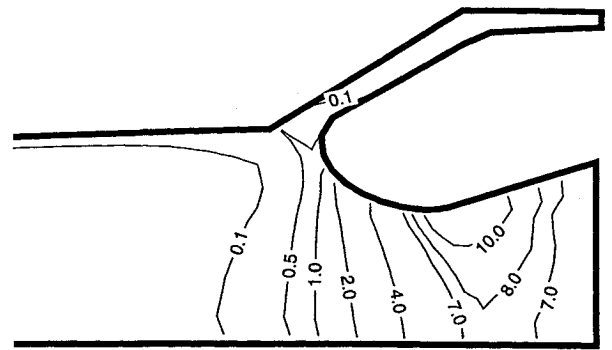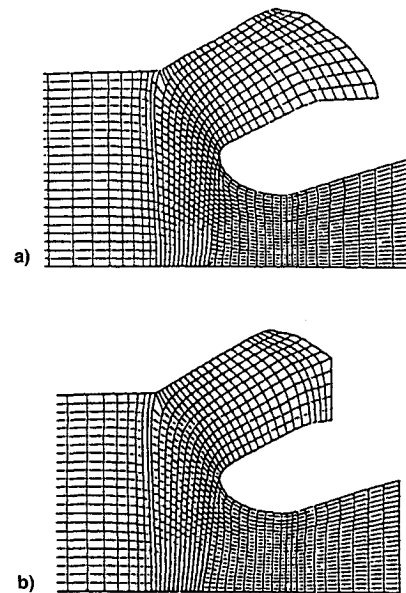

Fig. 13   Grid in aft end of Titan SRMU, with and without 216-mm slag pool at 55-s burnback: a) without slag pool b) with 216-mm slag pool.

metric effect of the SRMU slag pool, which does not appear to exceed 430 mm, is a reasonable approximation.

Another issue addressed is whether a motor undergoing flight acceleration will accumulate slag at a substantially different rate than during a static firing. All of the numerical results that have been presented so far were obtained for a gravitational acceleration of 9.8 m/s². It is reasonable to expect that the slag capture rate will increase at higher acceleration levels, especially for larger droplets, since the ratio of drag force to body force on a droplet varies as D^{-2}. To address this issue, a numerical solution was performed for a flow with 100-μm droplets at 55 s of burnback in a 3-g (29.4 m/s²) gravitational field; this acceleration is representative of the maximum level in flight. The slag accumulation rate for this 3-g solution differed from the 1-g solution by less than 1%. This result indicates that the acceleration effect will be fairly small for the accelerations and droplet sizes expected for the SRMU; consequently, the static firing slag results and the numerical results at 1 g should be applicable in flight.

Finally, we have investigated the possibility that a small change in the propellant grain design could reduce the total slag capture during the burn. Of primary interest were small changes that could be easily retrofitted to the current Titan SRMU design, rather than changes that would require a redesigned motor. Two such modifications (see Fig. 14) are as follows: 1) placing a short-lived inhibitor on the propellant

Table 3 Slag accumulation rates (kg/s) at 0-s
burnback with and without inhibitor

Droplet size, μm	Without inhibitor	With inhibitor	Change, %
35	26.6	26.6	——
60	43.9	41.7	−5
100	63.6	52.7	−17
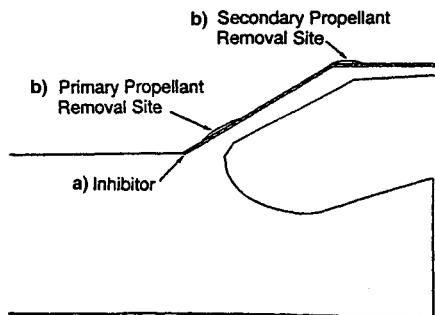
Fig. 14 Aft end of SRMU (0-s burnback) showing slag reduction concepts: a) inhibitor and b) propellant removal locations.

surface in the submerged nozzle region and 2) removing a small amount of propellant at two critical locations. In Fig. 8, the initial slag capture rate vs position along the outer nozzle wall is plotted for 100-μm droplet flow. The largest capture rates occur in the first cell adjacent to point T (see Fig. 2), and to a lesser degree in the ninth cell past point T, i.e., the first cell past the corner (see Fig. 2). One way to reduce the large slag capture at these two sites would be to remove some propellant, thereby increasing the surface separation at these crucial locations (Fig. 14). Of course, this has the associated disadvantage of decreasing the propellant load. The use of an inhibitor to reduce the slag capture also has an associated disadvantage, namely the weight of the inhibitor. Furthermore, the inhibitor must be designed to create a new burnback pattern for the propellant in the slot area, otherwise the large initial capture pattern of the present SRMU design simply would appear at a later time. Putting aside these objections for the present, we have considered two-phase flows of 35-, 60-, and 100-μm droplets in 0-s burnback motors, with the inhibitor of Fig. 14 in place. The numerical results for these solutions, along with corresponding results from Table 2 for no inhibitor, are found in Table 3. For 100-μm droplets, the effect of the inhibitor is to reduce the initial slag accumulation rate by 17%. The reasoning behind these slag reduction concepts proceeds from the observation, noted earlier in our discussion of the 60-μm accumulation rate curve, that the rate falls off early in the burn due to the declining importance of the surface proximity effect and rises late in the burn due to the widening of the slot mouth. Since the propellant surface must recede due to propellant burnback, there is little that can be done about the latter effect. However, modifications to the initial grain configuration in the slot region can reduce the large initial accumulation rate that results from the proximity effect. If a lower accumulation rate could be maintained for some time early in the burn, then a reduction in the total slag capture might be achieved.

Based on this result, it seems that a small reduction in the total slag capture, perhaps 1–10%, would be possible with this concept. However, it is unlikely that this amount would justify the additional weight of the inhibitor.

IV. Concluding Remarks

In this article, we have described a numerical calculation procedure for the analysis of slag accumulation in a solid rocket motor. The axisymmetric, two-phase flow calculations

are inviscid and rotational, but with full momentum and energy coupling between the phases, which are combustion gas and molten Al_2O_3 droplets. The inviscid treatment of the gasdynamic equations is an assumption. This assumption was originally motivated by earlier work[3] on the Payload Assist Module (PAM) motor, in which very close similarities were found between the viscous and inviscid flowfields (i.e., the size of the separated flow zone in the imbedded nozzle region was negligible). Having completed the present work, several remarks can be made about the inviscid assumption. Early in the motor burn, when the geometry is similar to Fig. 2, there is no flow separation and the inviscid model is adequate. Late in the firing (i.e., Fig. 3), experience with boundary-layer theory suggests that flow in the region surrounding the imbedded nozzle will separate and the imbedded region will contain one or more vortices. This raises two questions: Does the experience with boundary layers apply to flow in motors with imbedded nozzles? Is it necessary to correctly model all the details of the gasdynamics to get adequate engineering calculations of the slag capture? The answer to the first question is best obtained from experimental data. Water models of the Space Shuttle SRM aft end suggest that the flow surrounding the imbedded nozzle is both three dimensional and unsteady.[19] Reference 19 speaks of periodic flushing of the vortices in the dome. This flushing implies that the two-dimensional solution may move between an inviscid, unseparated solution and a viscous one with trapped vortices. Furthermore, any steady two-dimensional solution, viscous or inviscid, may not properly capture the physics of the gasdynamic flow. The second question can be addressed with the help of the numerics. Small differences in slag capture were found when a finite slag level was added as shown in Fig. 13. This suggests that changes to the gasdynamic flow and by implication the gasdynamic flow itself has a small effect on the slag capture. Finally, note that we have gotten good agreement with both the total amount of slag and the accumulation rate. Thus, the model presented herein is a good model for predicting slag capture. It is not claimed that it faithfully represents all the details of the gas flow in the imbedded region, which may be turbulent viscous, three dimensional, and/or unsteady.

The method presented here is sufficiently general for the analysis of slag capture in most, if not all, solid rocket motors. Although the code in its present form allows for only one unchanging liquid droplet size, this restriction is not inherent in the numerical technique. It could be removed if it were necessary to analyze a flow in which uniform droplet size clearly was a bad assumption; e.g., the flow inside the exit nozzle of solid rocket motor where droplet breakup reduces the droplet size. An important result is that slag capture is found to begin at the beginning of the firing; prior to this work, slag accumulation was thought to be confined to the final 30–50% of the burn.

We have applied this numerical calculation procedure to the analysis of slag accumulation in the Titan SRMU. The major results of this study, which it should be emphasized, are motor geometry dependent, and therefore, do not necessarily hold for motors other than the SRMU, are as follows:

1) The rate of slag capture is approximately constant during the burn, prior to motor tailoff.

2) The onboard slag mass and the depth of the slag pool increase (approximately) linearly with time, prior to motor tailoff.

3) The slag capture rate increases uniformly with Al_2O_3 droplet size.

4) The acceleration level (up to 3 g) has a negligible effect on the slag capture for reasonable Al_2O_3 droplet sizes, so that the slag accumulation will be the same in flight as in static firings.

5) When the most recent (and we assume best) experimental measurements available for Al_2O_3 droplet size distribution in

solid rocket motors[1] are used, this method predicts a total slag accumulation of 2265 kg, which agrees well with the data.[15]

6) Small propellant grain design changes that could be retrofitted to the current motor, such as tailoring the grain shape or temporarily inhibiting propellant burning in the submerged nozzle region, can reduce the initial slag accumulation rate and to some extent the total slag capture. However, the potential improvement is not large and comes at the expense of propellant loss (grain tailoring) or additional dead weight (inhibitor).

Acknowledgments

References

[1]Salita, M., "Quench Bomb Investigation of Al_2O_3 Formation from Solid Rocket Propellants (Part II): Analysis of Data," 25th JANNAF Combustion Meeting, Oct. 1988.

[2]Murdock, J. W., "Comment on "Simple Modeling of Particle Trajectories in Solid Rocket Motors," *Journal of Propulsion and Power*, Vol. 10, No. 3, 1994, pp. 437, 438.

[3]Misterek, D. L., Murdock, J. W., and Koshigoe, S., "Gas-Dynamic Flow in a Spinning, Coning Solid Rocket Motor," *Journal of Propulsion and Power*, Vol. 9, No. 1, 1993, pp. 35–42.

[4]Wang, J. C. T., and Widhopf, G. F., "A High-Resolution TVD Finite Volume Scheme for the Euler Equations in Conservation Form," *Journal of Computational Physics*, Vol. 84, No. 1, 1989, pp. 145–173.

[5]Wang, J. C. T., and Widhopf, G. F., "An Efficient Finite Volume TVD Scheme for Steady State Solutions of the 3-D Compressible Euler/Navier-Stokes Equations," AIAA Paper 90-1523, June 1990.

[6]Gilbert, M., Davis, L., and Altman, D., "Velocity Lag of Particles in Linearly Accelerated Combustion Gases," *Jet Propulsion*, Vol. 25,

Jan. 1955, pp. 26–32.

[7]Knudsen, J. G., and Katz, D. L., *Fluid Mechanics and Heat Transfer*, McGraw–Hill, New York, 1955, p. 511.

[8]Harten, A., "High Resolution Schemes for Hyperbolic Conservation Laws," *Journal of Computational Physics*, Vol. 49, No. 3, 1983, pp. 357–393.

[9]Thompson, J. F., Warsi, Z. U. A., and Mastin, C. W., *Numerical Grid Generation—Foundations and Applications*, Elsevier, New York, 1985.

[10]Murdock, J. W., "Rocket Thrust Perturbation from Discharge of an Inert Body," *Journal of Propulsion and Power*, Vol. 2, No. 2, 1986, pp. 117–123.

[11]Johnston, W. A., "A Numerical Procedure for the Analysis of the Internal Flow in a Solid Rocket Motor During the Ignition Transient Period," AIAA Paper 91-1655, June 1991.

[12]Nickerson, G. R., Culick, F. E. C., and Dang, A. L., "The Solid Propellant Rocket Motor Performance Computer Program (SPP) Version 6.0," Edwards AFB, AFAL-TR-87-078, CA, Dec. 1987.

[13]Dobbins, R. A., and Strand, L. D., "A Comparison of Two Methods of Measuring Particle Size of Al_2O_3 Produced by a Small Rocket Motor," *AIAA Journal*, Vol. 8, No. 9, 1970, pp. 1544–1550.

[14]Price, E. W., "Combustion of Metallized Propellants," *Fundamentals of Solid-Propellant Combustion*, edited by K. K. Kuo and M. Summerfield, Vol. 90, Progress in Aeronautics and Astronautics, AIAA, New York, 1984, pp. 479–513.

[15]Dolan, K. W., Curnow, G. M., Perkins, D. E., Schneberk, D. J., Costerus, B. W., La Chapell, M. J., Turner, D. E., and Wallace, P. W., "Real-Time Radiography of Titan IV Solid Rocket Motor Upgrade (SRMU) Static Firing Test QM-2," Lawrence Livermore National Lab., UCRL-CR-117148, May 1994.

[16]Reddall, W. F., "Volume vs. Depth Plots for SRMU Aft Dome," The Aerospace Corp., IOC 93(5442)FMD-WFR-79, March 1993.

[17]Rasmusser, J. J., and Nelson, R. P., "Surface Tension and Density of Molten Al_2O_3," *Journal of the American Ceramic Society*, Vol. 54, No. 8, 1970, pp. 398–401.

[18]Caveny, L. H., and Gany, A., "Breakup of Al/Al_2O_3 Agglomerates in Accelerating Flowfields," *AIAA Journal*, Vol. 17, No. 12, 1979, pp. 1368–1371.

[19]Waesche, R. H. W., and Sargent, W. H., "Space Shuttle Solid Rocket Motor Aft-End Internal Flows," *Journal of Propulsion and Power*, Vol. 5, No. 6, 1989, pp. 650–656.